

Robust Strategies for Automated AFM Force Curve Analysis—I. Non-adhesive Indentation of Soft, Inhomogeneous Materials

David C. Lin

Laboratory of Integrative and Medical Biophysics,
National Institutes of Health,
9 Memorial Drive, Bldg. 9 Rm. 1E118,
Bethesda, MD 20892
e-mail: lindavid@mail.nih.gov

Emilios K. Dimitriadis

National Institute of Biomedical Imaging and
Bioengineering,
National Institutes of Health,
13 South Drive, Bldg. 13 Rm. 3N17,
Bethesda, MD 20892
e-mail: dimitria@helix.nih.gov

Ferenc Horkay

Laboratory of Integrative and Medical Biophysics,
National Institutes of Health,
13 South Drive, Bldg. 13 Rm. 3W16,
Bethesda, MD 20892
e-mail: horkay@helix.nih.gov

The atomic force microscope (AFM) has found wide applicability as a nanoindentation tool to measure local elastic properties of soft materials. An automated approach to the processing of AFM indentation data, namely, the extraction of Young's modulus, is essential to realizing the high-throughput potential of the instrument as an elasticity probe for typical soft materials that exhibit inhomogeneity at microscopic scales. This paper focuses on Hertzian analysis techniques, which are applicable to linear elastic indentation. We compiled a series of synergistic strategies into an algorithm that overcomes many of the complications that have previously impeded efforts to automate the fitting of contact mechanics models to indentation data. AFM raster data sets containing up to 1024 individual force-displacement curves and macroscopic compression data were obtained from testing polyvinyl alcohol gels of known composition. Local elastic properties of tissue-engineered cartilage were also measured by the AFM. All AFM data sets were processed using customized software based on the algorithm, and the extracted values of Young's modulus were compared to those obtained by macroscopic testing. Accuracy of the technique was verified by the good agreement between values of Young's modulus obtained by AFM and by direct compression of the synthetic gels. Validation of robustness was achieved by successfully fitting the vastly different types of force curves generated from the indentation of tissue-engineered cartilage. For AFM indentation data that are amenable to Hertzian analysis, the method presented here minimizes subjectivity in preprocessing and allows for improved consistency and minimized user intervention. Automated, large-scale analysis of indentation data holds tremendous potential in bioengineering applications, such as high-resolution elasticity mapping of natural and artificial tissues. [DOI: 10.1115/1.2720924]

Keywords: atomic force microscopy, contact mechanics, elasticity, indentation

Introduction

The atomic force microscope (AFM) has become ubiquitous in biomedical sciences as a tool for characterizing topographical and elastic properties of biological and synthetic materials. The small tip size and control of tip-sample interactions make it possible to image subnanometer features. Unlike electron microscopes, samples being imaged can be immersed in liquid (e.g., physiological salt solution), allowing biological specimens to be maintained at or near their native conditions. Investigators have taken advantage of the force spectroscopy capabilities of the AFM, which has force sensitivity on the order of 10 pN, to probe the elasticity of materials that are very soft and exhibit inhomogeneity at microscopic scales and to study among many things, the stretching behavior of single molecules as well as inter- and intramolecular interactions (see, e.g., [1–7]).

When the cantilever tip is used as a nanoindenter, the AFM is well suited for probing the local elasticity of small, very soft, and inhomogeneous samples. It has been used to study the elasticity of bacteria [8], cells [9–12], endothelia [13], articular cartilage [14–16], and bony tissue [17]. However, despite its advantages over more conventional testing methodologies, data processing issues hinder the consistency of elasticity measurements on soft biological tissues and preclude the use of the AFM in large-scale

studies. Many of these issues are associated with the spatial variability of elastic properties and tip-sample interactions in microscopically inhomogeneous samples, which produce a diversity of force-displacement curves. A number of analysis techniques are utilized by investigators to identify the pertinent, linear elastic portion of each dataset and subsequently extract Young's modulus by fitting the data with a contact mechanics model [11,12,18–20]. However, attempts to automate these approaches have not proven to be successful in eliminating the need for subjective user input (e.g., specifying an estimate of the contact point based on visual inspection [19] or specifying the range of the noncontact region [11]) or capable of accurately processing diverse populations of curves. We have compiled a collection of complementary strategies that addresses the known issues in the analysis of AFM force curves, and implemented these strategies in a robust algorithm for extracting the elastic properties of soft, highly inhomogeneous tissue samples. These strategies allow automated analysis of large numbers of indentation datasets, thus offering a highly desirable tool for elasticity mapping of materials that exhibit inhomogeneity at microscopic scales. To validate the procedure, a comparison of results from AFM measurements and conventional macroscopic compression tests performed on polyvinyl alcohol (PVA) gels of known composition is presented. Additionally, tissue-engineered cartilage was probed at multiple locations along the surface to generate a set of visually distinct force curves consistent with the inhomogeneous nature of the biological tissue.

This paper focuses on the analysis of indentation data that exhibit Hertzian behavior (i.e., linear elastic with negligible adhe-

Contributed by the Bioengineering Division of ASME for publication in the JOURNAL OF BIOMECHANICAL ENGINEERING. Manuscript received June 12, 2006; final manuscript received November 15, 2006. Review conducted by Clark T. Tung.

Table 1 Terms of the generalized form of the force-indentation relation for various models

Model	λ	β
Hertz: sphere of radius R	$\frac{4ER^{1/2}}{3(1-\nu^2)}$	3/2
Sharp cone of tip angle 2ϕ (see Fig. 1)	$\frac{2E \tan \phi}{\pi(1-\nu^2)}$	2
Sharp pyramid of tip angle 2ϕ (see Fig. 1): Bilodeau solution [26]:	$\frac{1.4906E \tan \phi}{2(1-\nu^2)}$	2
Rico et al. solution [28]:	$\frac{E \tan \phi}{2^{1/2}(1-\nu^2)}$	2

ν is Poisson's ratio and E is Young's modulus

sive interactions, as in the approach curves of all experimental data sets presented). Extension of the strategies to non-Hertzian, adhesive contact [21–23] will be discussed in a separate paper. In the following sections, relevant force-indentation relationships derived from contact mechanics theories are first presented, followed by a summary of existing approaches for extracting the elastic properties of the indented material. Essential features of a comprehensive strategy are then outlined and the scheme devised by the authors is introduced. Next, typical experimental results are presented and discussed. The significance of a robust, automated procedure is reiterated in the concluding remarks.

Theory

Contact Mechanics Models. The classical problem of an elastic half-space indented by a rigid object was first treated by Hertz in 1881 and Boussinesq in 1885 [18]. Numerous others have contributed to the theoretical framework, which is widely used in interpreting the results of indentation tests at all length scales. Exact solutions in the form of force-indentation relationships, contact pressure distributions, and stress and displacement fields exist for axisymmetric indenter geometries (e.g., cylinder, sphere, and cone). By necessity, approximate solutions are derived in the case of more complex geometries, such as the pyramid. Many solutions of interest in the indentation of linear elastic materials can be represented by the generalized force-indentation relation [19,24],

$$F = \lambda \delta^\beta \quad (1)$$

where F is the force applied to the indenter and δ is the indentation depth. The term λ and exponent β are given in Table 1 for indenters that are spherical (from the original Hertz theory of contact between two ellipsoidal bodies and oftentimes referred to as the Hertz equation or model), sharp conical [5,25], or sharp-tipped pyramidal [26] in geometry. For typical tapered indenters with a blunt tip (Fig. 1), the relationship is [25,27,28]

$$F = \frac{2E}{1-\nu^2} \left\{ a\delta - m \frac{a^2}{\tan \phi} \left[\frac{\pi}{2} - \arcsin\left(\frac{b}{a}\right) \right] - \frac{a^3}{3R} + (a^2 - b^2)^{1/2} \left[m \frac{b}{\tan \phi} + \frac{a^2 - b^2}{3R} \right] \right\} \quad (2a)$$

where 2ϕ is the tip angle, b is the radius at which the tapered sides transition into a spherical tip of radius R , a is the contact radius, and the constant m has different values for the cone ($=\frac{1}{2}$) and the pyramid ($=2^{1/2}/\pi$). When $\delta < b^2/R$, the Hertz model applies. The contact radius is related to the indentation depth by

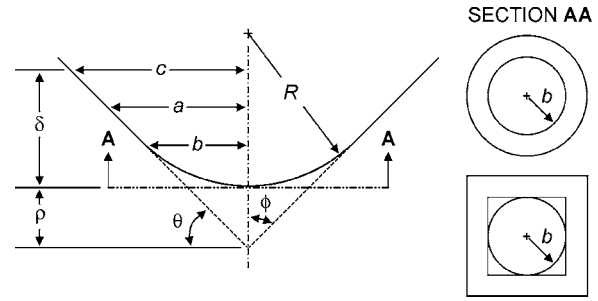


Fig. 1 Blunt and sharp tips of the same tip angle. Both conical and pyramidal tips are shown. Radius a is the contact radius and c is the indentation radius. The blunt tips transition at radius or half-width b to a round tip with radius R . The incline angle of the faces of the pyramid is represented by θ .

$$\delta + \frac{a}{R} [(a^2 - b^2)^{1/2} - a] - n \frac{a}{\tan \phi} \left[\frac{\pi}{2} - \arcsin\left(\frac{b}{a}\right) \right] = 0 \quad (2b)$$

with $n=1$ for the cone and $n=2^{3/2}/\pi$ for the pyramid. The sharp-tipped models are recovered when $R=b=0$ while the limiting case of $R \rightarrow \infty$ yields the solutions for truncated tips. Note that since a circle is used to approximate the area of contact of the pyramid in Eqs. (2a) and (2b), reduction to the sharp-tipped model produces results that differ slightly from the Bilodeau solution, which assumes a realistic square contact region (see Table 1).

Equations (1) and (2) describe what is commonly referred to as Hertzian indentation in which the interaction between tip and sample is due solely to the externally applied force. When significant adhesive forces exist between the contacting solids, they must be accounted for. Adhesive contact mechanics models will be discussed in a separate paper (Part II) [29].

Basic Approaches to Extracting Elastic Properties From AFM Data. Indentation is performed by moving the cantilever in the direction perpendicular to the sample surface, z , between a starting position, $z=0$, and an end position, $z=z_{\max}$. Regardless of tip geometry, the force of indentation is related to the stiffness and motion of the cantilever by

$$F = k_c(d - d_0) \quad (3)$$

where k_c is the spring constant of the cantilever, d is the measured deflection, and d_0 is the deflection offset at the point of contact between the indenter and the sample where the force is zero. The indentation depth δ is therefore given by

$$\delta = (z - z_0) - (d - d_0) = (z - d) - (z_0 - d_0) = w - w_0 \quad (4)$$

where z_0 is the translation of the cantilever at the contact point. The transformed variable $w=z-d$ (computed from the raw, d versus z , data) and its value at the contact point, w_0 , are introduced for simplification [18]. Together with Eqs. (1) or (2), Eqs. (3) and (4) allow fitting of contact mechanics models to AFM indentation data.

The simplest fitting approach is to select the contact point (z_0, d_0) by visually inspecting the force-displacement curve. The portion of the data representing the noncontact region is then discarded and regression analysis is used to fit the data (z, d) with the appropriate contact mechanics model to obtain the value of Young's modulus. Alternatively, a Young's modulus value can be calculated for each point in the indentation region [18]. The point-wise calculations of E will tend toward a constant value that is dependent on the chosen contact point. Typically, Poisson's ratio is assumed to be 0.5 for soft, gel-like materials [5,20,30]. To avoid uncertainties about the compressibility of the sample, some researchers define an elastic constant incorporating the terms E and $(1-\nu^2)$, thereby combining the linear elastic and compressibility properties of the sample into a single material constant [31–33].

Table 2 Strategies for objectively extracting linear elastic properties from AFM data

Method	Description	Deficiencies
Constrained sequential search [18]	Fit contact model to each (z, d) pair and select best fit Fitting parameters: E	Contact point may not be located on curve Contact point must lie within ramp
Semi-constrained sequential search	Similar to sequential search, but only z coordinate is specified at each iteration Fitting parameters: E, d_0	Contact point must lie within ramp
Unconstrained sequential search	Similar to sequential search, but the first (z, d) pair in each iteration is input as the initial guess Fitting parameters: E, z_0, d_0	Contact point must lie within ramp
Extrapolation of first derivative of cantilever deflection [12]	Contact is assumed to occur when the change in deflection with respect to piezoposition is zero Fitting parameters: E	Extrapolation may not be precise if derivative is not well behaved in the contact region For spherical indenters, fitting of derivative requires very good initial estimates of parameters
Derivatives of cantilever deflection [20]	Initial contact occurs at maximum change in deflection with respect to piezoposition Fitting parameters: E	Large uncertainties when signal-to-noise is high or when sample is soft Contact point may not be located on curve
Average deflection in noncontact region [11]	Set d_0 equal to the average value of d in the noncontact region Fitting parameters: E, z_0	Contact point must lie within ramp Need to identify noncontact region Large uncertainties when signal-to-noise is high or when sample is soft
Power series correction [19]/ Taylor series expansion	Contact model is expanded in a two-term power series about an arbitrary point in the vicinity of the contact point Fitting parameters: E, d_0	Contact point must lie within ramp Ambiguity and subjectivity in the selection of assumed contact point Inclusion of data from noncontact region will bias results

Note: The first four strategies are most amenable to automation. The first two strategies form the basis of our comprehensive scheme.

Objective Schemes for Extracting Elastic Properties.

A-Hassan et al. introduced an automated, contact point independent technique to generate relative elasticity maps by showing that the relative work of indentation at some force is proportional to the relative measure of stiffness [31]. However, an absolute measure of elastic properties requires fitting of force-indentation data to contact mechanics models. Since both F and δ are dependent on the contact point, objective approaches to optimally estimating the contact point are necessary; the features of a number of these techniques are summarized in Table 2 and discussed below.

One type of approach restricts the contact point to be a member of the dataset and henceforth will be referred to as the constrained approach. Nyland and Maughan [20] devised a method using the first and second derivatives of the cantilever deflection with respect to the piezodisplacement. After smoothing the data curve, the data point corresponding to the maximum value of the second derivative or to the extrapolated point of zero first derivative is chosen as (z_0, d_0) . For probing very soft materials in which the cantilever deflection is small, even small levels of noise can greatly affect calculations of the derivatives and introduce large errors. Hence, the second derivative method is limited in its applicability.

In sequential or linear search schemes, the candidate contact point is marched (either directly or indirectly, depending on the variation) along the force-displacement curve. The point that produces the best least-squares fit of the indentation data is selected as the solution. Note that the derivative and visual inspection methods generate comparatively poorer fits because the contact point in those noniterative methods is determined without considering its effect on the quality of fit. We have identified three variations of sequential search (see the first three entries in Table 2). The constrained variation is best suited for data with low levels of noise because it selects the contact point from among the collected dataset. No probe-sample long-range interactions are assumed to

exist. Dimitriadis et al. [18] employed this variant to demonstrate that selection of the contact point by subjective visual inspection produces fits that may differ significantly from those obtained by objectively selecting the best contact point through a methodical search procedure.

In the semi-constrained variation of sequential search, the z coordinate at each iteration is chosen from the acquired z -position vector and the corresponding d_0 along with E are the fitting parameters. Finally, neither z_0 nor d_0 is fixed in the unconstrained variant of the fitting procedure. Rather, the (z, d) pair is used as the initial guess in the regression analysis. In a noniterative scheme proposed by Radmacher [11], d_0 is estimated by averaging the range of d values over the noncontact region, leaving z_0 and Young's modulus E as the fitting parameters. This approach can be considered the semi-constrained counterpart to the visual inspection method and is likewise prone to error when noise levels are high.

Kolambkar [19] formulated a more rigorous unconstrained approach by evaluating the error associated with assuming an incorrect contact point. He expanded the resulting force-indentation relation in a power series in $(d_1 - d_0)$, where d_1 is the d coordinate of the assumed contact point (z_1, d_1) chosen from within the neighborhood of the contact point. We developed a variation of Kolambkar's scheme with less ambiguity in the selection of (z_1, d_1) by making use of the transformed variable w and expanding the generalized equation in a Taylor series about some value of cantilever deflection d_1 arbitrarily chosen from the contact region. A major disadvantage of the power series methods is that they are extremely sensitive to the inclusion of data from the noncontact region (i.e., attempting to fit contact mechanics models to a data set that contains a substantial number of points from the noncontact region will weaken the fit of the contact portion).

Up to this point, the methods discussed all require the contact

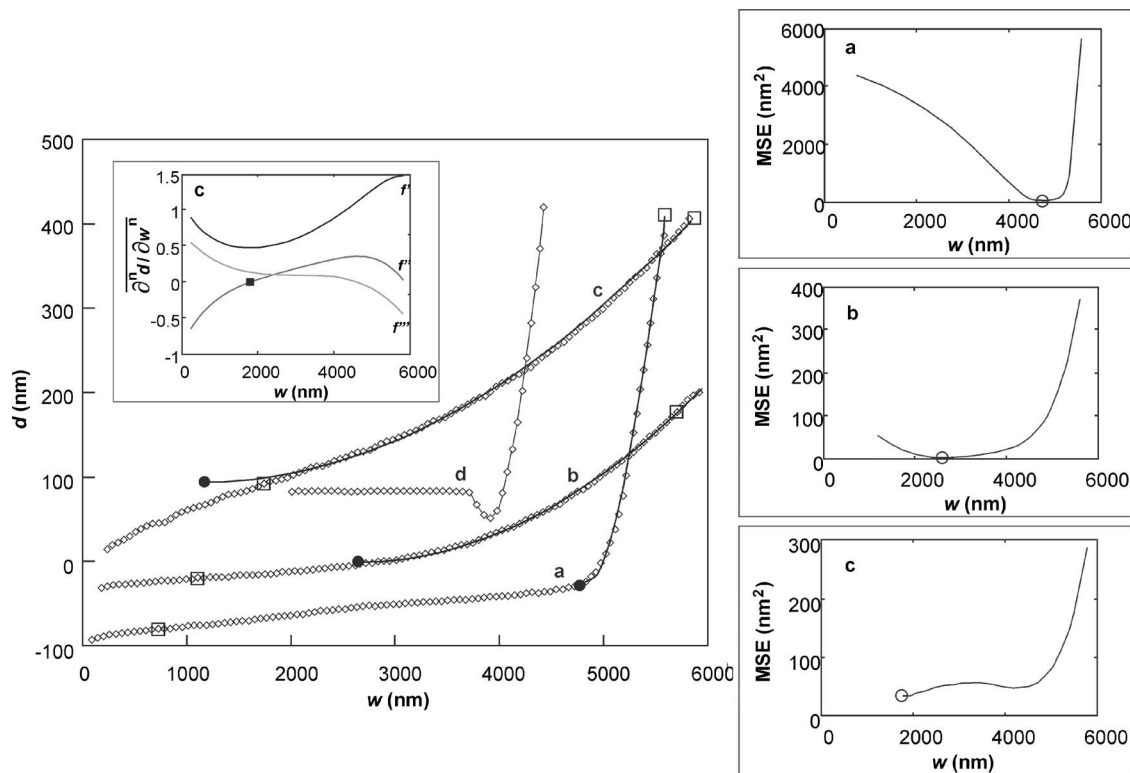


Fig. 2 (a)–(c): Force curves (open diamonds), best-fit curves (solid lines) and corresponding plots of the MSE as a function of position of the assumed contact point. Three separate indentations of cartilage specimens are presented. The portion of each curve bracketed by the \square symbols is the linearly elastic region identified during data preprocessing. For ease of visualization, curves were shifted vertically with no effect on the solutions. When the contact point (indicated by \bullet) lies within the range of the retained data, the MSE plot is unimodal (curves “a” and “b”). When the contact point lies outside the range of the retained data, the MSE plot does not have a global minimum; in this example (curve “c”), tip-sample interactions (not adhesive in nature) obscured the location of the contact point by distorting the initial contact portion of the force curve. The inset in the large plot shows the first, second, and third derivatives of deflection d with respect to w for curve “c.” Each derivative is normalized such that the difference between the maximum and minimum value is one. The cutoff point ($f''=0$ and $f'''>0$) is indicated by \blacksquare . (d): A representative force-displacement curve showing significant adhesive interactions.

point to be bracketed by the endpoints of the dataset (i.e., $0 < z_0 < z_{\max}$). In certain instances, however, the contact point may not even be captured within the data set or may be situated in a portion of the data that exhibits non-Hertzian behavior. The former condition is most likely to occur in the indentation of very soft materials (Young’s modulus < 1 kPa), where the cantilever deflection at the onset of contact may not be discernible from the real-time deflection versus piezodisplacement (d versus z) plot. Consequently, it may be difficult to determine an appropriate ramp starting position that brackets the contact point. The latter condition is usually attributable to the existence of tip-sample interactions; it is necessary here to make a distinction between adhesive and nonadhesive interactions. Adhesive interaction is easily identified by a decrease or dip in cantilever deflection from the equilibrium, zero-load position as the tip approaches the surface of the sample (i.e., the direction of deflection is opposite that during indentation; see curve “d” in Fig. 2). In the forthcoming paper, various models of adhesive contact will be examined. Large, non-adhesive tip-sample interactions present an ill-defined complication—the contact point may be situated in a portion of the curve that exhibits nonlinearity, as shown by curve “c” in Fig. 2. Elimination of such data (e.g., by truncating the dataset at the inflection point) may result in the exclusion of the contact point from the retained data set. We now introduce a rearward search scheme that allows accurate fitting of such previously intractable data sets. The method is essentially a semi-constrained sequential search using smoothed data to minimize the effect of noise. At

each step, the value of the assumed z_0 from the previous iteration is decremented by the z spacing in the original data. The search is halted once no further improvement to the least-squares fit of the retained data is detected.

Jaasma et al. [12] formulated a derivative-based approach that removes the need for subjective input and serves as a good alternative to the search strategies under certain conditions. This method differs from that of Nyland and Maughan [20] in that the solution is derived by evaluating data from the contact region, thereby eliminating bias from the high levels of noise and nonlinearity commonly observed in the vicinity of the contact point. The method is discussed in greater detail in Appendix A.

Integration of Strategies for Automation. Using a single objective approach in an automated fitting routine will not consistently produce acceptable results because each approach has deficiencies with respect to certain types of data sets. The basic requirement of a comprehensive scheme for extracting elastic properties from indentation data is the capability to accurately process the data regardless of whether the contact point is situated within the retained dataset. Hence, at least one of the objective approaches in Table 2 should be integrated with the rearward search method. There is wide latitude in the choice and sequence of the methods incorporated into the comprehensive scheme. However, we eliminated the power-series methods despite their requirement of only a single function evaluation because of the inaccuracy associated with including points from the noncontact

region. We also chose to exclude the first derivative extrapolation method because of the difficulties in applying it in conjunction with the Hertz equation (discussed in Appendix A). The sequential search methods are ideally suited for automation because they eliminate the need for subjective user intervention. Discussed briefly in the next paragraph are the particularities of each variant that should be considered in their integration into a comprehensive strategy.

As with all methods that restrict the contact point to the set of the collected data points, the constrained sequential search approach is greatly influenced by noise. When significant noise or long-range probe-sample interactions are present, the contact point may lie some distance away from the collected data points; constraining the solution to the dataset may produce large errors. This variant is therefore suitable for locating the vicinity of the contact point. The unconstrained and semi-constrained search strategies provide improved accuracy at the expense of increased complexity associated with greater numbers of fitting parameters. The semi-constrained approach is preferred because it is less computationally intensive. Based on the level of noise in the data, one may choose to impose lower and upper bounds in the formulation of the semi-constrained problem to limit the deviation of the contact point from the data. However, the chief advantage of applying the semi-constrained method without bounds is that it is amenable to efficient search techniques (e.g., the Golden Section search). We elected to implement the bounded method in our comprehensive strategy for this reason.

Design of Algorithm for Extraction of Young's Modulus. Detailed in this section is the integrative strategy we developed with the goal of maximizing computational efficiency in the analysis of large collections of indentation datasets (up to 1024 force-displacement curves in a single collection). The algorithm, which is represented by the flowchart in Fig. 3, has been implemented in *Mathematica* (Wolfram Research, Champaign, IL) and *MATLAB* (MathWorks, Natick, MA), and includes routines for data preprocessing and addressing uncertainties in tip geometry.

A cursory fitting process using the following steps is first performed to determine whether significant adhesive interactions are present:

1. Marching along the data set, the initial portion (assumed noncontact region) is fit with a line while the latter portion is fit with a power function of the form

$$d = d^{(i)} + b(w - w^{(i)})^{3/2} \quad (3')$$

where b is the lone fitting parameter, i is the current iteration, and the exponent of $3/2$ is characteristic of Hertzian indentation with a rigid sphere (Table 1). Hence, $(w^{(i)}, d^{(i)})$ takes on all values between the first ($i=1$) and last points. In the adopted convention, the last point refers to the point of maximum indentation, regardless of whether extension or retraction data are considered.

2. At each iteration, an aggregate mean square error (MSE) is calculated, with the contribution from the nonlinear fit given greater weight to offset the typically low MSE values from the zero-force, noncontact region. In most cases, multiplying the MSE of the nonlinear fit by a factor of 2 is sufficient. However, if the noncontact region comprises a disproportionately large segment of the data, a larger factor (e.g., 10) is necessary to identify the best fit to the contact region. The linear fit associated with the lowest aggregate MSE is used as the preliminary check for the presence of adhesive forces—a negative slope using either factor indicates that such interactions are potentially present. If the slopes using both factors are positive, Hertzian analysis is applied and the $(w^{(i)}, d^{(i)})$ pair corresponding to the lowest MSE, denoted (w^*, d^*) , is used as an approximate contact point to calculate the strain at maximum indentation. It is necessary to employ

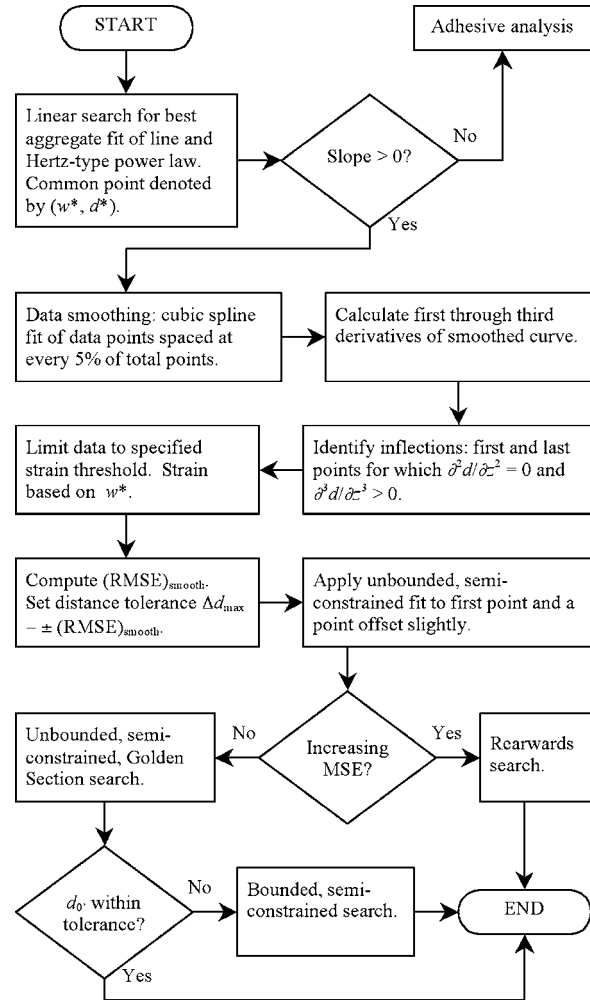


Fig. 3 Flowchart representation of the algorithm

the Johnson-Kendall-Roberts (JKR) and associated adhesive contact models [21–23] if the slopes are negative.

If Hertzian analysis is applicable, data preprocessing is carried out to identify and trim spurious portions of the curves. A smoothing operation is performed by fitting cubic splines to a subset of the complete dataset (e.g., we use a spacing of 5% of the total number of points). Alternative smoothing methods (e.g., low-pass filtering) may be applied. From the smoothed curve, first order ($\partial d / \partial w$) through third-order derivatives are obtained. Inflection points are then identified by evaluating second and third derivatives along the curve (e.g., zeros of the second derivative with a corresponding positive third derivative is an upturn in the curve; see inset to the large plot in Fig. 2). Convex inflections near the beginning of the curve (e.g., curve “c” in Fig. 2) are indicative of nonadhesive tip-sample interactions. Costa and Yin have shown numerically that solutions derived using linear elasticity theory produce large errors when applied to materials that exhibit nonlinear behavior [25]. The preprocessing step is therefore also necessary to identify and remove contributions from such nonlinear effects.

Nonlinearities may appear after some depth of indentation due to experimental factors (e.g., use of a cantilever of insufficient stiffness, sample defects, such as rigid inclusions, and contribution from the underlying substrate caused by small sample thickness); their existence is confirmed by an inflection near the point of maximum cantilever deflection. After truncating the data set, nonlinearities caused by material-dependent phenomenon, such as

strain hardening and softening may still exist. If the strain threshold at which the linear assumption breaks down is known, it can be used to further limit the range of data to be analyzed. For a spherical indenter of radius R , the normal strain ε_{zz} is [18]

$$\varepsilon_{zz} = \frac{2a}{\pi R(1-\nu)} \quad (5)$$

where the contact radius a is equal to $(R\delta)^{1/2}$ and the approximate indentation is $\delta = w - w^*$. The position w_{lim} at which the specified strain limit ε_{lim} occurs is therefore

$$w_{\text{lim}} = w^* + \left[\frac{\pi \varepsilon_{\text{lim}} R^{1/2} (1-\nu)}{2} \right]^2 \quad (6)$$

In the final preprocessing step, the level of noise in the data is determined by computing the root-mean-square error (RMSE) of the smoothed fit. This value, which we denote by $(\text{RMSE})_{\text{smooth}}$ is used to define the *distance tolerance*, i.e., set an upper bound of allowable deviation of the contact point from the original data curve. In the algorithm, the difference in cantilever deflection between the contact point and the curve (Δd) is computed, with the tolerance set to $\Delta d_{\text{max}} = \pm (\text{RMSE})_{\text{smooth}}$.

Following preprocessing, the unbounded, semi-constrained sequential search procedure is implemented. Using the MSE as a measure of goodness of fit, points from the beginning of the retained data to the current assumed contact point are fitted with a straight line while the remaining points are fitted with the appropriate contact model. The linear fit is necessary to maintain consistency in the total number of data points; goodness-of-fit measures are prone to improve as the size of the dataset decreases. We first determine the existence of a viable solution (i.e., whether the contact point is bracketed by the endpoints of the data set). If a viable solution exists (condition 1), the MSE is a well-behaved, unimodal function of the assumed z_0 (see curves “a” and “b” Fig. 2). Otherwise, the MSE demonstrates an initially increasing trend with the assumed z_0 (condition 2; curve “c” in Fig. 2). This latter condition is exploited in the evaluation by comparing the MSE at the first point and a point offset from it by a small distance.

It is important to note that the well-behaved manner in which the MSE varies with the assumed z_0 is characteristic of the *unbounded* semi-constrained search method, making it the method of choice when computational efficiency is desired. Under condition 1 of this implementation, a Golden Section search is applied to find a viable solution (E_0, z_0, d_0). If the contact point does not exceed the distance tolerance, no further processing is necessary. Otherwise, a bounded semi-constrained search is performed in the vicinity of z_0 . We find for our data that a spread of roughly 200 nm centered about z_0 is sufficient. The range of d_0 at each iteration is limited to $(d - \Delta d_{\text{max}} < d_0 < d + \Delta d_{\text{max}})$. Imposing bounds on the deviation of the contact point further ensures accuracy in the force-indentation behavior (i.e., when the deviation of the contact point from the data curve is small, there will be virtually no indentation force at the onset of contact).

Under condition 2, the rearward search is invoked. The first local minimum in MSE encountered during the search procedure is the solution. A detail worthy of mention is that in rare cases, the contact point lies so far outside the range of the retained data that the MSE function becomes unimodal. We detect such instances by comparing the MSE of solution returned by the Golden Section or bounded semi-constrained search to that of the smoothed fit. If the former value exceeds the latter by a large margin (~ 1.5 times), the rearwards search is executed.

The steps outlined above are also applicable to blunt conical and pyramidal indenters. Following the procedure set forth in Appendix B, the data is first fit to a generalized quadratic equation. The corresponding sharp tip model can then be used to approximate the elastic properties of the sample.

Materials and Methods

Preparation of PVA Gels. PVA gels were prepared by first dissolving 56 g of PVA (molecular weight 70,000–100,000; Sigma) in 344 ml of deionized water at 99°C. The final concentration of the stock solution was 14% (w/w). Gels were made by crosslinking the PVA in aqueous solution with glutaraldehyde (GDA) at pH ~ 1.5 . The pH was adjusted by HCl. To create samples of increasing stiffness, the PVA concentration was increased while maintaining a constant crosslink density (one unit of GDA per 100 units of vinyl alcohol) [34]. Gel cylinders and thick layers (2 mm to > 1 cm) with final PVA concentrations of 3%, 6%, 9%, and 12% (w/w) were cast in molds (1 cm diam and 1 cm high) and 35 mm Petri dishes, respectively. All samples were stored in deionized water until testing.

Direct Compression Test of PVA Cylinders. A texture analyzer bench top materials testing system (Stable Micro Systems, UK) was used to perform load-controlled compression of the gel cylinders at a ramp speed of 1 mm/s. For all samples (at least three of each concentration), the shear modulus was determined from the rubber elasticity equation [35,36]

$$\sigma = G(\Lambda - \Lambda^{-2}) \quad (7)$$

where σ is the normal component of the engineering, or nominal, stress (force per undeformed area); G is the shear modulus; and Λ is the deformation ratio ($=L/L_0$, where L and L_0 are the deformed and undeformed lengths, respectively). The undeformed dimensions of each cylinder were measured using a micrometer. The absence of volume change and barreling during the compression measurements was checked.

Preparation of Tissue-Engineered Cartilage Specimens. Details on the growth of cartilaginous tissue from chondrocytes isolated from chick embryo sternum have been described previously by Horkay et al. [37]. Briefly, the chondrocytes were seeded on PVA disks (25 mm diam and 2 mm thick) and cultured for durations of up to 30 days. The tissue layer was removed from the surface of the PVA gel at the end of the culture period and sectioned transversely. Thin (~ 1 mm) pieces of tissue were glued to glass cover slips using a cyanoacrylate adhesive (Loctite, Rocky Hill, CT), with the sectioned surface exposed. The specimens were stored at 0°C until testing.

AFM Nanoindentation of PVA Films and Cartilage Specimens. Nanoindentation of samples was performed using a commercial AFM (Bioscope I with a Nanoscope IIIA controller, Veeco Instruments, Santa Barbara, CA) seated atop an inverted optical microscope. General purpose, oxide-sharpened silicon nitride tips with square pyramidal geometry, incline angles of 55 deg (see Fig. 1), and 10 nm nominal tip radius were used (model DNP-S, Veeco). The cantilevers were modified by gluing either a 9.6 μm dia polystyrene bead or a 5.5 μm dia glass bead near the tip. The 3% gel required a much more compliant cantilever (0.06 N/m nominal spring constant) than the other gels (0.58 N/m nominal spring constant). The spring constant of each cantilever was determined using the thermal tune method [38,39]. The algorithm outlined previously was used to extract Young's modulus from each dataset.

Multiple force curves for each PVA film were collected using the “force-volume” mode of the AFM. In this automated raster scanning method, the user defines the size of the square region to be scanned, the resolution, and the relative trigger threshold (i.e., the maximum cantilever deflection). Because the gels were assumed to be relatively homogeneous, the resolution was set to the lowest limit of 16×16 indentations covering a $20 \mu\text{m} \times 20 \mu\text{m}$ region. Relative trigger thresholds were set to either 100 nm or 50 nm. For each sample, at least two regions spaced over 1 cm apart were scanned. The 9% gel was chosen to test the high-resolution force-volume scanning capability of the instrument;

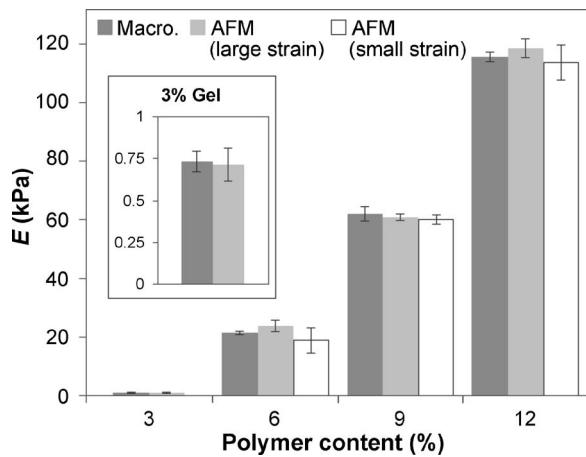


Fig. 4 Results of macroscopic compression and AFM indentation tests on PVA gels. Due to the large difference in sample size between AFM and macroscopic measurements, error bars show standard deviation rather than standard error. Inset shows data for the 3% gel in larger scale. Large strain AFM values were obtained by including points up to maximum indentation. Small strain values were obtained by truncating the data at ~20–25% strain.

one of the scans was set to a resolution of 32×32 indentations covering a region of $50 \mu\text{m} \times 50 \mu\text{m}$. To avoid problems that may be caused by deviations of the sample surface from the horizontal, we set the ramp size to the maximum allowed by each piezoscanner. This ensured that the tip was fully clear of the surface following the last indentation of a raster line and as it was moved $20 \mu\text{m}$ or $50 \mu\text{m}$ to the beginning of the next line.

Cartilage samples were equilibrated to room temperature and allowed to swell to equilibrium in phosphate-buffered saline (pH 7.4). Indentations were performed along a linear direction by offsetting the tip successively by $2.5 \mu\text{m}$ to $5 \mu\text{m}$. The ramp size and start position were adjusted as necessary to accommodate changes in topography and load-deflection behavior.

Results and Discussion

Results of the macroscopic compression and AFM nanoindentation tests on the PVA gels shown in Fig. 4 demonstrate reasonable agreement across a broad range of mechanical compliances equivalent to that found in soft biological tissues. It is obvious

from Fig. 4 that an initial polymer content of 3% is close to the gelation threshold of this system. Furthermore, the nonlinear scaling of Young's modulus with the polymer content is attributable to the increased amount of entanglements frozen into the network as more polymer chains are introduced. In the cylindrical samples of the 6%, 9%, and 12% gels, no corrections for the end conditions were deemed necessary because no barrel distortion was observed. However, the 3% gels were not self-supporting, with significant compression even in the absence of an external load; stresses and deformation ratios were therefore calculated from estimated dimensions. Hence, the accuracy of the macroscopic test results for the 3% gels are suspect because of uncertainties in the end conditions and undeformed dimensions. In contrast, nanoindentation of the samples posed no untoward difficulties, making the AFM a good alternative for measuring the bulk elastic properties of very soft materials.

In the analysis of the AFM data, the PVA gels were assumed to be incompressible based on experimental results reported in the literature (ν slightly < 0.5 for PVA swollen in water) [40] and on generally accepted macroscopic properties of rubberlike materials [41]. Likewise, the cartilage samples were assumed to be incompressible under the test conditions because each indentation occurred too rapidly for liquid to be forced from the specimens; Mow et al. found the instantaneous Poisson's ratio of articular cartilage to indeed be 0.5 [42]. Indentation results for the cartilage specimens are plotted as a function of probe position in Fig. 5.

Adhesive tip-sample interactions were observed in many instances as the AFM tip was retracted. Hence, tip retraction data for the PVA gels and cartilage specimens are not presented here. As alluded to in prior sections, analysis of such curves requires non-Hertzian models and will be discussed in detail in a later paper.

The applicability of linear elastic models to biological tissues and cells is an unresolved issue in AFM nanoindentation. Clearly, large strains are capable of causing substantial deviations from linear behavior [18] although the existence and limit of the linear regime is intrinsic to the probed material. In the PVA gels, maximum strains approaching 50% were attained with no visually detectable detriment to the quality of the Hertzian fits. However, limiting the strains to ~20–25% resulted in a decrease in the average Young's modulus (for the results plotted in Fig. 4, the overall decrease was ~12%) as well as the MSE (overall decrease of ~66%, due to a large reduction in the number of data points fitted), revealing the existence of strain stiffening. The increase in the standard deviations of Young's modulus can be ascribed to the loss in resolution due to truncation of a significant portion of each

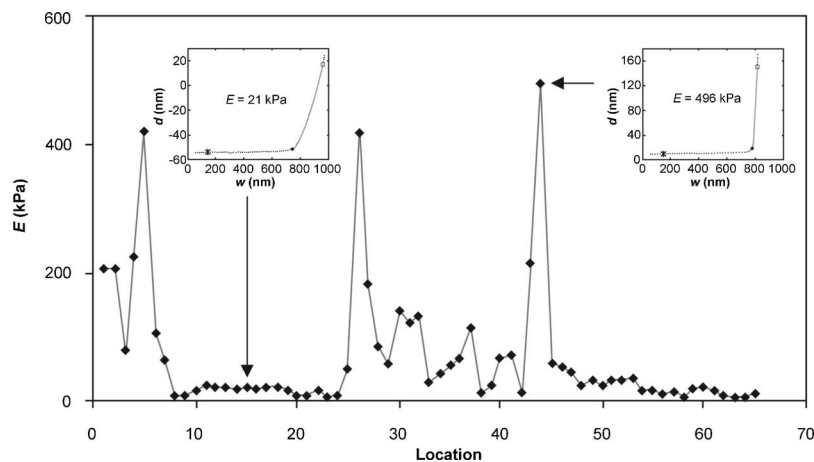


Fig. 5 Sample plot of Young's modulus of tissue-engineered cartilage as a function of position along a line. Points were spaced $\sim 2.5 \mu\text{m}$ apart. Regions of very low stiffness most likely are chondrocytes. Insets show sample curve fits.

data set. When the indentation depth at which the linear assumption becomes invalid is unknown, it is therefore judicious to perform a preliminary analysis to establish a baseline of cantilever deflection in order to prevent excessive truncation. Maximum strains in the cartilage datasets were all <30%, and no truncation was performed based on the MSE values.

Differences of ~15% were found in the two sets of Young's moduli extracted from the 12% PVA sample (mean±standard deviation: 139.48±3.29 kPa and 118.46±3.26 kPa). We attribute this to the coincidence of the first set of 16×16 indentations with a region of high polymer concentration. In biological materials such as cartilage, local variations in mechanical properties are detected by performing multiple measurements throughout the region of interest. To estimate the bulk properties from local measurements, a statistically significant number of measurements are required over a large area. This usually entails the use of software-controlled automation of the AFM data collection process. For this purpose, an automated algorithm to process the large number of datasets is necessary. Our analysis of the force-volume datasets, one of which contained 1024 curves, demonstrated the great benefit of a robust, automated procedure. The measurements on cartilage were of low resolution by intent and performed for the purpose of demonstrating the capability of the algorithm to accurately process a diverse population of curves. We now have the means to process high-resolution force-volume datasets of inhomogeneous samples.

A significant component of the algorithm is the rearward search strategy, which addresses the issue of extracting the Young's modulus of materials for which the contact point is not captured in the ramp or is far removed due to nonadhesive tip-sample interactions. We found the frequency of such occurrences to be significant (~5%) in the cartilage data. Hence, a scheme that does not provide for this contingency cannot be considered robust. The approach was validated by truncating several data sets to remove the contact point, applying the rearward search, and evaluating the accuracy as a function of the number of truncated points. In a simulated dataset with perfectly fitted data, the error in Young's modulus was negligible despite the number of points truncated. For actual datasets, the error increased with the amount of noise in the data and as more points were excluded; errors generally did not exceed 5%.

Of all tip geometries, blunt pyramidal indenters are perhaps the most widely used. Their advantage in mechanical probing lies in the capability to concurrently produce high-resolution images (with resolution dependent on the tip radius). However, the approximate analytical solution given by Eq. (2) is difficult to apply directly to experimental data. In lieu of the flawed approach of approximating the tip as either a sphere or a sharp cone, some researchers generate calibration curves by combining nanoindentation with macroscopic test methods [15]. The alternative approach introduced in Appendix B makes use of sharp tip models for dealing with blunt indenters and complements the strategies in our algorithm. Applied in reverse order, the technique can be used as a calibration method for estimating tip radii by scanning a sample of known compliance; the procedure is described in Appendix C. These methods provide a means of using common, tapered tips to measure the elasticity of soft samples. The reader is cautioned that the assumption of small strains intrinsic to the contact mechanics theory used in deriving Eqs. (1) and (2) is easily violated with sharply tapered tips [18,26]. Hence, use of pyramidal indenters in elasticity measurement should be reserved for situations requiring imaging of the probed region.

In general, poor data resulting from experimental conditions and/or improper technique present difficulties in data fitting. The many variables include sample preparation and tip selection to minimize interactions; calibration of cantilever stiffness k_c (many researchers use the nominal value provided by the manufacturer, but uncertainties can be quite large and since E is directly proportional to k_c , large

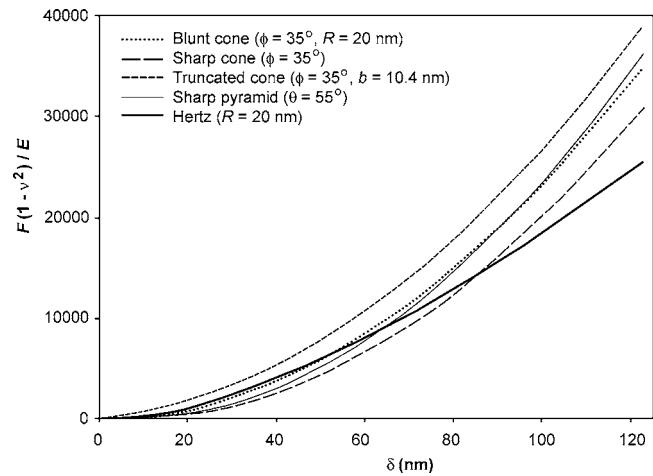


Fig. 6 Simulated force-indentation curves for tips of various geometries. Forces are normalized against material properties of the indented half space.

errors in the extracted moduli can result from using incorrect values); and setting of ramp size and ramp starting position. Of equal importance are the geometry and dimensions of the indenter. Although the effects of tip shape and radius on AFM images are now well understood, their effects on elasticity measurements have not received the same level of attention. The common practice of applying the Hertz model [16,43] for indentation with blunt pyramidal tips is generally erroneous in the probing of soft materials because most commercial pyramidal tips have nominal tip radii on the order of 10–20 nm, whereas maximum indentation depths of up to several hundred nanometers are typical in such samples. Figure 6 shows simulated force curves for the various geometries listed in Table 1. Clearly, the equations are not interchangeable (e.g., the Hertz solution does not accurately model indentation by a pyramidal tip). Assuming a sharp conical or pyramidal tip [11,17,30,39,44–46] is also ill-advised in many situations because it introduces significant errors even for small tip radii (refer to Fig. 7 for simulations of the effect of tip radius for a blunt conical indenter). Corrections for the discrepancy in force-indentation behavior between sharp and blunt tips, such as the scheme proposed

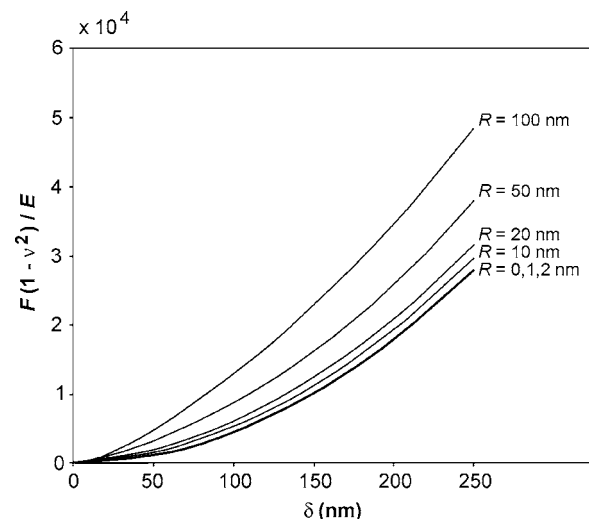


Fig. 7 Simulated force-indentation curves for blunt conical tips of various tip radii. The curves are nearly parallel beyond a certain indentation depth and at small radii, are virtually indistinguishable from one another.

in Appendix B, can reduce the error significantly but result in greater computational expense. An additional complication in the use of tapered tips to measure elastic properties is the potential damage or alteration to the tip geometry subsequent to indenting a hard surface [47], required for instance, to calibrate the voltage-deflection sensitivity. Care must be exercised to minimize the contact force when performing these calibrations.

Uncertainties associated with the aforementioned variables preclude quantitative comparisons of measurements using different cantilevers and are likely a source of the large discrepancies in reported values of Young's modulus for various soft biological materials. In the interest of achieving consistency and accuracy in absolute measurements of elastic properties, it is necessary to utilize the calibration methods available for determining cantilever stiffness [38,39,48,49] and tip geometry [50–53].

Although the strategies discussed here have been applied to contact mechanics models dealing with the indentation of an infinite half-space, they are readily applicable to models that account for the effects of finite sample thickness. Dimitriadis et al. [18] derived force-indentation relations suitable for thin samples and used the constrained sequential search method in fitting their data. Determination of the need to apply the modified models is based on knowledge of the sample thickness in relation to the maximum indentation depth.

Conclusions

The potential of the AFM in high-throughput local elasticity measurements has not been realized due to the lack of robust, automated data processing schemes. The strategies presented here are valid for the analysis of indentation data that can be assumed to obey the fundamental conditions of the Hertz theory (i.e., material isotropy and homogeneity at the length scale of the probe, small indentation depth and probe size relative to sample size, and deformations that do not exceed the linear stress-strain regime). These strategies, when combined systematically as illustrated in the sample algorithm, address the known issues in fitting elastic contact models to AFM force curves, and eliminate subjectivity in the determination of Young's moduli. High-resolution elasticity maps exemplify how the capabilities of the AFM can be more fully exploited with the availability of automated data fitting. Combined with the judicious selection of indenter geometry, choice of contact model, and proper calibration techniques, it is feasible to produce accurate AFM elasticity measurements using tips of various shapes and sizes.

Acknowledgment

This work was supported by the Intramural Research Program of the NIH/NICHD.

Appendix A: Method Based on Extrapolation of the First Derivative

The method developed by Jaasma et al. [12] requires smoothing of the force-displacement curve and calculating the first derivative of the cantilever deflection with respect to the piezoposition. Substituting Eqs. (3) and (4) into Eq. (1) and then differentiating with respect to w gives the mathematical basis of the method

$$k_c(d - d_0) = \lambda(w - w_0)^\beta \quad (\text{A1})$$

$$\frac{\partial d}{\partial w} = \frac{\beta\lambda}{k_c}(w - w_0)^{\beta-1} \quad (\text{A2})$$

It is obvious from Eq. (A2) that the derivative is zero at the point of contact. In probing whole cells using microspheres, Jaasma et al. found that the force-displacement behavior did not follow the Hertz model ($\beta=3/2$), but instead followed a parallel-spring recruitment model ($\beta=2$). For such a relationship, Eq. (A2) is linear. Hence, Jaasma and colleagues were able to fit lines to pre-defined regions of interest within the contact region and then

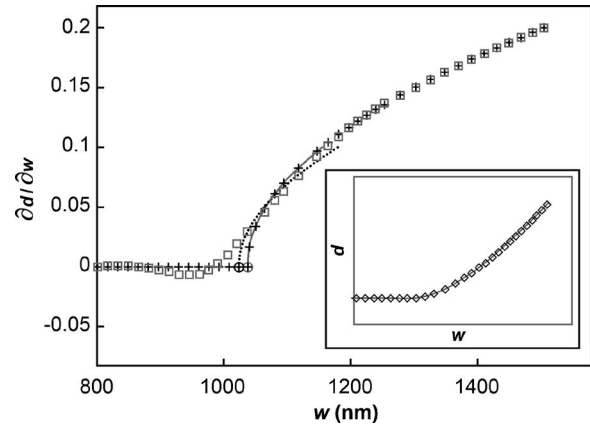


Fig. 8 Plot of the first derivative ($\partial d / \partial w$) for a simulated curve (indicated by +) that obeys the Hertz equation and for the same curve after performing a smoothing operation using splines (indicated by \square). Predicted contact points (indicated by \circ) are from fits to the region of interest in the range 10–40% of the maximum value of $\partial d / \partial w$ (solid line for the simulated data and dotted line for the smoothed data). Note the deviation in the behavior of the derivative after smoothing and the concomitant degradation in the fit, resulting in an early predicted point of contact. The inset shows the simulated d vs. w data (indicated by \diamond ; range of d : –122 to –59 nm) and the smoothed fit (solid line).

extrapolate the lines to $\partial d / \partial w = 0$ in order to estimate w_0 . The regions of interest were set as the range over which the derivative was 0–15% and 10–40% of its extreme value at or close to maximum indentation depth. The predicted w_0 corresponding to the greater cantilever extension was selected. Depending on whether an actual point within the dataset is selected as the contact point, this approach may be applied as either a constrained or semi-constrained method in the subsequent regression analysis. Note that it can also be used as an alternative to the unbounded, semi-constrained search procedure that we implement as a preliminary step to check the existence of a viable solution—if the extrapolated contact point falls beyond the range of the dataset, a rearward search will be necessary.

The extrapolation method can be adapted for analyzing curves that obey the Hertz model by replacing the linear fitting function with a power law of exponent 1/2. Although $\partial d / \partial w$ transitions abruptly from a horizontal line to a convex curve at the point of contact for an ideal curve, in actual data with some level of noise, error propagation associated with the smoothing, differentiation, and fitting operations may introduce an inflections in $\partial d / \partial w$ and significantly bias the extrapolation. This is illustrated in Fig. 8 for a simulated dataset generated using the Hertz equation. Based on this shortcoming, we do not recommend this approach for precise detection of the contact point when spherical indenters are used. It can, however, be substituted for the preliminary semi-constrained search process; used for that purpose, a quadratic function, for which the quality of initial estimates of fitting parameters is much less stringent, may be used to fit the derivative in the regions of interest.

Appendix B: Strategy for Analyzing AFM Curves Obtained Using Blunt Tips

Figure 6 shows simulated force curves for the various geometries represented listed in Table 1. Clearly, the equations are not interchangeable (e.g., the Hertz solution does not accurately model indentation by a pyramidal tip). The effect of tip radius for a blunt conical indenter can be seen in Fig. 7. Without resorting to numerical methods or approximate solutions to the contact mechanics problem, we show that the sharp pyramid model can be

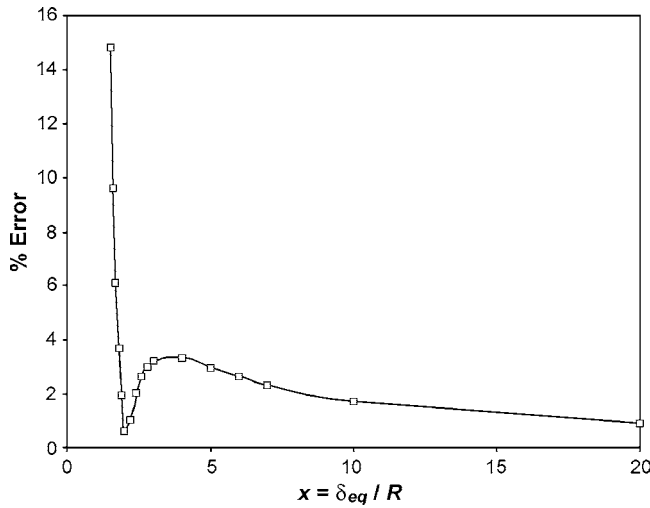


Fig. 9 Error in force as a function of the ratio of equivalent deflection to tip radius

used with minimal error to the analysis of indentation with a blunt pyramid when the correction presented here is applied.

Starting with sharp and blunt tips of identical opening angle β , we note that a much larger indentation is required with the sharp tip in order to achieve the same contact radius a . We introduce the equivalent deflection δ_{eq} , defined as the indentation with the sharp tip for which the indentation radii for both tips are equal to c (see Fig. 1). From basic geometric relations,

$$\delta_{eq} = \delta + \rho = \delta + \frac{b}{\tan \phi} - R + \sqrt{R^2 - b^2} \quad (B1)$$

where ρ is the difference in depth between the two tips for the same indentation radius c . For a given indentation δ with the blunt tip, the sharp-tipped model can be used to approximate the force-indentation behavior by using the equivalent deflection. The range of deflections for which the approximation is valid, expressed as a multiple of blunt tip radius, is shown in Fig. 9. The error in force reaches a minimum of 0.65% at $\delta_{eq} = 2R$ and does not exceed 4% for $\delta_{eq} > 2R$. Errors in Young's modulus (not shown) are comparable. The use of the equivalent deflection allows the use of a simple relation, i.e., Eq. (1) to model the indentation mechanics of a geometrically more complex tip.

This approach is conducive to automation by using the strategies discussed. To apply it in practice:

1. Note that Eq. (2a) can be approximated by a generalized quadratic. Hence, the contact point can be found by fitting the data to the equation $F = \xi \delta^2 + \gamma \delta$, where ξ and γ are coefficients to be determined along with (z_0, d_0) .
2. Once the contact point is determined, the data can be expressed in terms of F versus δ or F versus δ_{eq} .
3. From the transformed data retain only the points for which $\delta_{eq} \geq 2R$. These points represent the portion of the curve that matches well with the shape of the curve for the sharp tip. The curve of F versus δ should now be nearly parallel with the curve for the sharp tip.
4. To account for the shifts in the curve from that for the sharp tip, refit the data with a quadratic of the most generalized form, $F = q\delta^2 + \kappa\delta + \chi$, where κ and χ account for the horizontal and vertical shifts and $q \approx \lambda$.
5. E can be calculated from the following relationships:

$$E \approx \frac{\pi q(1 - \nu^2)}{2 \tan \phi} \quad (\text{blunt cone}) \quad (B2)$$

$$E \approx \frac{1.4906q}{2 \tan \theta(1 - \nu^2)} \quad (\text{blunt pyramid}) \quad (B3)$$

Appendix C: Finding the Radius of a Blunt Tip by Indenting a Calibration Sample of Known E

In order to apply the strategy described in Appendix B, the radius of the tip must be known. Direct (e.g., electron microscopy) and indirect (e.g., AFM imaging of well-defined grids) calibration methods exist, but may not be readily available. The approach presented here can be applied by indenting a calibration sample of known stiffness. Ideally, multiple indentations are performed on a homogeneous sample, and the mean of the results is taken as the tip radius. The procedure is as follows:

1. Obtain a force curve and fit it to the equation $F = \xi \delta^2 + \gamma \delta$ in order to find the contact point.
2. The fitted curve is used to compare with the theoretical curve for the sharp tip, which is of the form $F = \lambda \delta_{eq}^2$. Hence, calculate the true value of λ from the known E using Table 1.
3. Solving for R in Eq. (9) using the substitutions $\delta_{eq} = 2R$ and $b = R \cos \phi$, we obtain

$$R = \frac{\delta}{3 - 1/\sin \phi} \quad (C1)$$

4. Iteratively assume each successive value of δ to be the equivalent indentation $\delta_{eq} = 2R$. At each iteration I , calculate the approximate value of λ using $F = \lambda_I \delta_{eq}^2$.
5. The error in λ (i.e., $|\lambda - \lambda_I|$) follows the trend shown in Fig. 9. The value of δ corresponding to the minimum of the error is used to find the radius of the tip (R) using Eq. (12).

References

- [1] El Kirat, K., Burton, I., Dupres, V., and Dufrene, Y. F., 2005, "Sample Preparation Procedures for Biological Atomic Force Microscopy," *J. Microsc.*, **218**(Pt 3), pp. 199–207.
- [2] Fotiadis, D., Scheuring, S., Muller, S. A., Engel, A., and Muller, D. J., 2002, "Imaging and Manipulation of Biological Structures With the AFM," *Micron*, **33**(4), pp. 385–397.
- [3] Greulich, K. O., 2005, "Single-Molecule Studies on DNA and RNA," *ChemPhysChem*, **6**(12), pp. 2458–2471.
- [4] Kienberger, F., Ebner, A., Gruber, H. J., and Hinterdorfer, P., 2006, "Molecular Recognition Imaging and Force Spectroscopy of Single Biomolecules," *Acc. Chem. Res.*, **39**(1), pp. 29–36.
- [5] Radmacher, M., 1997, "Measuring the Elastic Properties of Biological Samples With the AFM," *IEEE Eng. Med. Biol. Mag.*, **16**(2), pp. 47–57.
- [6] Silva, L. P., 2005, "Imaging Proteins With Atomic Force Microscopy: An Overview," *Curr. Protein Peptide Sci.*, **6**, pp. 387–395.
- [7] Simon, A., and Durrieu, M., 2006, "Strategies and Results of Atomic Force Microscopy in the Study of Cellular Adhesion," *Micron*, **37**, pp. 1–13.
- [8] Schaar-Zammaretti, P., and Ubbink, J., 2003, "Imaging of Lactic Acid Bacteria With AFM—Elasticity and Adhesion Maps and Their Relationship to Biological and Structural Data," *Ultramicroscopy*, **97**(1–4), pp. 199–208.
- [9] Almqvist, N., Bhatia, R., Primbs, G., Desai, N., Banerjee, S., and Lal, R., 2004, "Elasticity and Adhesion Force Mapping Reveals Real-Time Clustering of Growth Factor Receptors and Associated Changes in Local Cellular Rheological Properties," *Biophys. J.*, **86**(3), pp. 1753–1762.
- [10] Hutter, J. L., Chen, J., Wan, W. K., Uniyal, S., Leabu, M., and Chan, B. M., 2005, "Atomic Force Microscopy Investigation of the Dependence of Cellular Elastic Moduli on Glutaraldehyde Fixation," *J. Microsc.*, **219**(Pt 2), pp. 61–68.
- [11] Radmacher, M., 2002, "Measuring the Elastic Properties of Living Cells by the Atomic Force Microscope," *Methods Cell Biol.*, **68**, pp. 67–90.
- [12] Jaasma, M. J., Jackson, W. M., and Keaveny, T. M., 2006, "Measurement and Characterization of Whole-Cell Mechanical Behavior," *Ann. Biomed. Eng.*, **34**(5), pp. 748–758.
- [13] Mathur, A. B., Collinsworth, A. M., Reichert, W. M., Kraus, W. E., and Truskey, G. A., 2001, "Endothelial, Cardiac Muscle and Skeletal Muscle Exhibit Different Viscous and Elastic Properties as Determined by Atomic Force Microscopy," *J. Biomech.*, **34**(12), pp. 1545–1553.
- [14] Radhakrishnan, P., Lewis, N. T., and Mao, J. J., 2004, "Zone-Specific Micro-mechanical Properties of the Extracellular Matrices of Growth Plate Cartilage," *Ann. Biomed. Eng.*, **32**(2), pp. 284–291.
- [15] Stolz, M., Raiteri, R., Daniels, A. U., VanLandingham, M. R., Baschong, W., and Aebi, U., 2004, "Dynamic Elastic Modulus of Porcine Articular Cartilage Determined at Two Different Levels of Tissue Organization by Indentation-

- Type Atomic Force Microscopy," *Biophys. J.*, **86**(5), pp. 3269–3283.
- [16] Tomkoria, S., Patel, R. V., and Mao, J. J., 2004, "Heterogeneous Nanomechanical Properties of Superficial and Zonal Regions of Articular Cartilage of the Rabbit Proximal Radius Condyle by Atomic Force Microscopy," *Med. Eng. Phys.*, **26**(10), pp. 815–822.
- [17] Tao, N. J., Lindsay, S. M., and Lees, S., 1992, "Measuring the Microelastic Properties of Biological Material," *Biophys. J.*, **63**, pp. 1165–1169.
- [18] Dimitriadis, E. K., Horkay, F., Maresca, J., Kachar, B., and Chadwick, R. S., 2002, "Determination of Elastic Moduli of Thin Layers of Soft Material Using the Atomic Force Microscope," *Biophys. J.*, **82**(5), pp. 2798–2810.
- [19] Kolambkar, Y. M., 2004, "Extracting Mechanical Properties of Cells/Biomaterials Using the Atomic Force Microscope," Master's thesis, University of Cincinnati, Cincinnati, <http://www.ohiolink.edu>
- [20] Nyland, L. R., and Maughan, D. W., 2000, "Morphology and Transverse Stiffness of Drosophila Myofibrils Measured by Atomic Force Microscopy," *Biophys. J.*, **78**(3), pp. 1490–1497.
- [21] Derjaguin, B. V., Muller, V. M., and Toporov, Y. P., 1975, "Effect of Contact Deformations on the Adhesion of Particles," *J. Colloid Interface Sci.*, **53**, pp. 314–326.
- [22] Johnson, K. L., Kendall, K., and Roberts, A. D., 1971, "Surface Energy and the Contact of Elastic Solids," *Proc. R. Soc. London, Ser. A*, **324**, pp. 301–313.
- [23] Muller, V. M., Yushchenko, V. S., and Derjaguin, B. V., 1980, "On the Influence of Molecular Forces on the Deformation of an Elastic Sphere and Its Sticking to a Rigid Plane," *J. Colloid Interface Sci.*, **77**(1), pp. 91–101.
- [24] Butt, H., Capella, B., and Kappl, M., 2005, "Force Measurements with the Atomic Force Microscope: Technique, Interpretation and Applications," *Surf. Sci. Rep.*, **59**, pp. 1–152.
- [25] Costa, K. D., and Yin, F. C. P., 1999, "Analysis of Indentation: Implications for Measuring Mechanical Properties With Atomic Force Microscopy," *ASME J. Biomech. Eng.*, **121**, pp. 462–471.
- [26] Bilodeau, G., 1992, "Regular Pyramid Punch Problem," *ASME J. Appl. Mech.*, **59**, pp. 519–523.
- [27] Na, S., Sun, Z., Meininger, G. A., and Humphrey, J. D., 2004, "On Atomic Force Microscopy and the Constitutive Behavior of Living Cells," *Biomech. Model. Mechanobiol.*, **3**(2), pp. 75–84.
- [28] Rico, F., Roca-Cusachs, P., Gavara, N., Farre, R., Rotger, M., and Navajas, D., 2005, "Probing Mechanical Properties of Living Cells by Atomic Force Microscopy With Blunted Pyramidal Cantilever Tips," *Phys. Rev. E*, **72**(2 Pt 1), pp. 021914.
- [29] Lin, D. C., Dimitriadis, E. K., and Horkay, F., 2007, "Robust Strategies for Automated AFM Force Curve Analysis—II. Adhesion-Influenced Indentation of Soft, Elastic Materials," *ASME J. Biomech. Eng.*, accepted for publication.
- [30] Domke, J., and Radmacher, M., 1998, "Measuring the Elastic Properties of Thin Polymer Films With the Atomic Force Microscope," *Langmuir*, **14**, pp. 3320–3325.
- [31] A-Hassan, E., Heinz, W. F., Antonik, M. D., D'Costa, N. P., Nageswaran, S., Schoenenberger, C., and Hoh, J. H., 1998, "Relative Microelastic Mapping of Living Cells by Atomic Force Microscopy," *Biophys. J.*, **74**, pp. 1564–1578.
- [32] Sun, Y., Akhremitchev, B., and Walker, G. C., 2004, "Using the Adhesive Interaction between Atomic Force Microscopy Tips and Polymer Surfaces to Measure the Elastic Modulus of Compliant Samples," *Langmuir*, **20**, pp. 5837–5845.
- [33] Touhami, A., Nysten, B., and Dufrene, Y. F., 2003, "Nanoscale Mapping of the Elasticity of Microbial Cells by Atomic Force Microscopy," *Langmuir*, **19**, pp. 4539–4543.
- [34] Horkay, F., and Nagy, M., 1980, "Elasticity of Swollen Polyvinyl Alcohol and Poly(Vinyl Acetate) Networks," *Polym. Bull. (Berlin)*, **3**(8–9), pp. 457–463.
- [35] Aklonis, J. J., and MacKnight, W. J., 1983, *Introduction to Polymer Viscoelasticity*, Wiley, New York.
- [36] Treloar, L. R. G., 1975, *The Physics of Rubber Elasticity*, Oxford University Press, London.
- [37] Horkay, F., Horkayne-Szakaly, I., and Basser, P. J., 2005, "Measurement of the Osmotic Properties of Thin Polymer Films and Biological Tissue Samples," *Biomacromolecules*, **6**(2), pp. 988–993.
- [38] Burnham, N. A., Chen, X., Hodges, C. S., Matei, G. A., Thoreson, E. J., Roberts, C. J., Davies, M. C., and Tendler, S. J. B., 2003, "Comparison of Calibration Methods for Atomic-Force Microscopy Cantilevers," *Nanotechnology*, **14**, pp. 1–6.
- [39] Hutter, J. L., and Bechhoefer, J., 1993, "Calibration of Atomic-Force Microscope Tips," *Rev. Sci. Instrum.*, **64**(7), pp. 1868–1873.
- [40] Urayama, K., Takigawa, T., and Masuda, T., 1993, "Poisson's Ratio of Poly-(Vinyl Alcohol) Gels," *Macromolecules*, **26**(12), pp. 3092–3096.
- [41] Geissler, E., and Hecht, A. M., 1980, "The Poisson Ratio in Polymer Gels," *Macromolecules*, **13**, pp. 1276–1280.
- [42] Mow, V. C., Lai, W. M., and Holmes, M. H., 1982, "Advanced Theoretical and Experimental Techniques in Cartilage Research," *Biomechanics: Principles and Applications*, Huiskes, R., Van Campen, D., and Dewijn, J., eds., Martinus Nijhoff, The Hague, pp. 47–74.
- [43] Nie, H. Y., Motomatsu, M., Mizutani, W., and Tokumoto, H., 1996, "Local Elasticity Measurement on Polymers Using Atomic Force Microscopy," *Thin Solid Films*, **273**, pp. 143–148.
- [44] Alcaraz, J., Buscemi, L., Grabulosa, M., Trepate, X., Fabry, B., Farre, R., and Navajas, D., 2003, "Microrheology of Human Lung Epithelial Cells Measured by Atomic Force Microscopy," *Biophys. J.*, **84**(3), pp. 2071–2079.
- [45] Jiao, Y., and Schaffer, T. E., 2004, "Accurate Height and Volume Measurements on Soft Samples With the Atomic Force Microscope," *Langmuir*, **20**, pp. 10038–10045.
- [46] Rotsch, C., Jacobson, K., and Radmacher, M., 1999, "Dimensional and Mechanical Dynamics of Active and Stable Edges in Motile Fibroblasts Investigated by Using Atomic Force Microscopy," *Proc. Natl. Acad. Sci. U.S.A.*, **96**(3), pp. 921–926.
- [47] Kopycinska-Muller, M., Geiss, R. H., and Hurley, D. C., 2006, "Contact Mechanics and Tip Shape in AFM-Based Nanomechanical Measurements," *Ultramicroscopy*, **106**(6), pp. 466–474.
- [48] Cumpson, P. J., Hedley, J., Clifford, C. A., Chen, X., and Allen, S., 2004, "Microelectromechanical System Device for Calibration of Atomic Force Microscope Cantilever Spring Constants Between 0.01 and 4 N/M," *J. Vac. Sci. Technol. A*, **22**(4), pp. 1444–1449.
- [49] Torii, A., Sasaki, M., Hane, K., and Okuma, S., 1996, "A Method for Determining the Spring Constant of Cantilevers for Atomic Force Microscopy," *Meas. Sci. Technol.*, **7**(2), pp. 179–184.
- [50] Jarausch, K. F., Stark, T. J., and Russell, P. E., 1996, "Silicon Structures for in Situ Characterization of Atomic Force Microscope Probe Geometry," *J. Vac. Sci. Technol. B*, **14**(6), pp. 3425–3430.
- [51] Li, Y., and Lindsay, S. M., 1991, "Polystyrene Latex Particles as a Size Calibration for the Atomic Force Microscope," *Rev. Sci. Instrum.*, **62**(11), pp. 2630–2633.
- [52] Markiewicz, P., and Goh, M. C., 1995, "Atomic Force Microscope Tip Deconvolution Using Calibration Arrays," *Rev. Sci. Instrum.*, **66**(5), pp. 3186–3190.
- [53] Vesenka, J., Manne, S., Giberson, R., Marsh, T., and Henderson, E., 1993, "Colloidal Gold Particles as an Incompressible Atomic Force Microscope Imaging Standard for Assessing the Compressibility of Biomolecules," *Biophys. J.*, **65**(3), pp. 992–997.